Materials Advances

ROYAL SOCIETY OF CHEMISTRY

PAPER

View Article Online
View Journal | View Issue

Cite this: *Mater. Adv.*, 2025, **6**, 8670

Fibrillization *versus* coacervation in arginine–tryptophan repeat peptides: effects of sequence length and pH

Valeria Castelletto,[a] Lucas de Mello,[a] Jani Seitsonen[b] and Ian W. Hamley *[a]

In peptides, alternating sequences of hydrophobic and hydrophilic residues in general promote β-sheet formation. On the other hand, liquid–liquid phase separation (LLPS) *via* self-coacervation is observed for certain peptides that can have a lower degree of sequence order due to specific intermolecular interactions (electrostatic, π-stacking, cation–π and others). Here, we explore the interplay between fibril formation and LLPS in aqueous solution for tryptophan–arginine repeat peptides $(WR)_n$ with n = 2–5. Peptide conformations are probed using a combination of spectroscopic methods and X-ray diffraction while self-assembly is studied through cryo-TEM, laser scanning confocal microscopy (LSCM), optical microscopy and small-angle X-ray scattering (SAXS). The pH-dependent aggregation is a particular focus. We find a general trend for extended nanotape structures to be favoured upon increasing the number of (WR) repeats. Coacervate droplets are observed due to LLPS for $(WR)_2$ and $(WR)_3$ at pH 12, whereas twisted nanotapes are formed by $(WR)_4$ and $(WR)_5$. Hydrogel formation is also observed at sufficiently high concentration at pH 12 for $(WR)_n$ with n = 3–5. In contrast at lower pH, we find that $(WR)_2$ forms micelles or globular aggregates whereas extended β-sheet structures (fibrils or nanotapes) are observed for the longer sequences. The cytocompatibility of all five sequences was determined using an MTT assay on human dermal fibroblast cells, and this revealed that the peptides are well tolerated by these cells at low concentrations. Our results reveal the remarkable pH-dependent phase behaviour of these model alternating peptides and we elucidate conditions for LLPS in short model $(WR)_2$ and $(WR)_3$ peptides.

Received 4th September 2025,
Accepted 17th October 2025

DOI: 10.1039/d5ma01006c

rsc.li/materials-advances

Introduction

It is understood that β-sheet formation of peptides is favoured by alternating sequences of hydrophobic and hydrophilic residues. In early work, this led to the peptide EAK16, AEAEAKAKAEAEAKAK, which is a region of hydrophobic and hydrophilic residues found in the yeast protein Zuotin.[1] The Zhang group built on this work by developing related peptides with different charge sequence patterns, as well as analogous peptides such as RAD16, RARARARADADADADA.[2,3] This led to the development of the 3D cell culture hydrogel peptide PuraM atrix™ which consists of the 16-mer peptide RADA16 $(RADA)_4$.[4] Saiani's group has further developed related peptides such as FEFKFEFK[5–7] and related sequences or VEVKVEVK, VKVKVEVK *etc.*[8] and explored the role of charge and its distribution on structural and mechanical properties as well as potential applications including slow release of drugs encapsulated in hydrogels.[8] In another example, the β-sheet formation of peptides containing alternating sequences of phenylglycine and Glu or Lys has been compared for a series of analogues.[9] The charge distribution and ion complementarity influence the morphology of the fibres formed, as well as the properties of fibrillar hydrogels formed by several peptides. The peptide EFEFKFEK has been used as a scaffold in variants with terminal tyrosine residues to produce β-sheet forming peptides that form hydrogels.[10] These self-assembling peptides also influence the inflammatory response of macrophages. Antiparallel β-sheets are produced in basic pH solutions of the β-hairpin MAX-1 peptide which contains $(VK)_4$ repeats linked *via* aV^DPPT tetrapeptide to induce a β-turn.[11] The peptide forms hydrogels and aggregation can be switched by pH since at low pH, the charge on the lysine residues hinders aggregation. This peptide has been used as a scaffold in many further developments, for example by tuning the sequence, peptides that can gel cell culture medium (DMEM) can be created.[12,13] In fact, charged residues are not essential in alternating peptide sequences that aggregates, since for example silk comprises aliphatic GAGA repeats forming ordered β-sheet domains.[14]

[a] *School of Chemistry, Food Biosciences and Pharmacy, University of Reading, Whiteknights, Reading RG6 6AD, UK. E-mail: I.W.Hamley@reading.ac.uk*
[b] *Nanomicroscopy Center, Aalto University, Puumiehenkuja 2, FIN-02150 Espoo, Finland*

Generally, peptide fibrils are formed through a nucleation and growth process of monomers or oligomers.[15–18] However, it has recently been reported that in some cases, peptide fibrils can nucleate from coacervate droplets formed by liquid–liquid phase separation (LLPS) a process described as a multistep desolvation process of the peptides confined within the droplets.[19–21] The nucleation of peptide fibrils from coacervate droplets has been observed for example for Fmoc-A[22,23] or Fmoc-H[22] [where Fmoc denotes fluorenylmethyloxycarbonyl]. The formation of fibrils inside liquid condensates resulting from LLPS has been reported for a three-component system consisting of two amyloid peptides and ATP (adenosine triphosphate).[24] The LLPS-mediated self-assembly of clusters and extended peptide structures such as nanosheets and nanotubes was exemplified for using a porphyrin–peptide conjugate containing the diphenylalanine peptide.[20] The formation of hydrogels with distinct fibril networks (and hence mechanical properties) mediated by initial LLPS was studied using carboxybenzyl-protected diphenylalanine (z-FF).[19]

The alternating peptide RFRFRFRF (*i.e.* $[RF]_4$) (R: arginine, F: phenylalanine) was shown to form β-sheet fibrils.[25] The fibrils coexist with globular aggregates, revealed by TEM and AFM, while X-ray fibre diffraction provided an orthorhombic structure of interdigitated layers. In a later systematic study of the effect of the number of repeats in $[RF]_n$ peptides with n = 1–5, it was demonstrated that solutions containing peptides with four or five repeats show clear evidence of β-sheet fibrillization, in contrast to the shorter sequences form irregular fractal-like aggregate clusters.[26] In a related study, the β-sheet self-assembly in $(EF)_4$ was examined in detail.[27] SAXS and AFM were used to elucidate the aggregation pathway which was found to occur *via* the initial formation small oligomers, followed by coalescence into nanofibrils and nanotapes.

We recently reported on the self-coacervation of W_2R_2 and W_3R_3 peptides in basic solutions, arising from π–π and cation–π interactions of the tryptophan residues.[28] The complex coacervation of the shorter peptide WR with ATP was also noted. Here, we investigate the conformation and self-assembly of the series $(WR)_{n=1-5}$ (Scheme 1) to explore the influence of the number of alternating repeats on the peptide self-assembly. These alternating model peptides are of considerable interest as they are the first, to our knowledge, to show a sequence-length dependent transition from LLPS to fibril formation. The conformation is probed using circular dichroism (CD) and FTIR spectroscopy while a range of microscopic methods (cryo-TEM, cryo-SEM and LSCM) complemented with SAXS (along with SAXS/WAXS and fibre XRD) are used to determine the self-assembled nanostructure. The peptides in this study with longer alternating sequences of non-aromatic and aromatic residues, are expected to undergo β-sheet formation. However, basic pH conditions favour LLPS for $(WR)_4$ and $(WR)_5$, as for the shorter homologues. In addition to studying the conformation and morphology, we also ascertained conditions for hydrogel formation, and performed preliminary studies of cytocompatibility for these peptides as feasibility tests for future bioactivity studies.

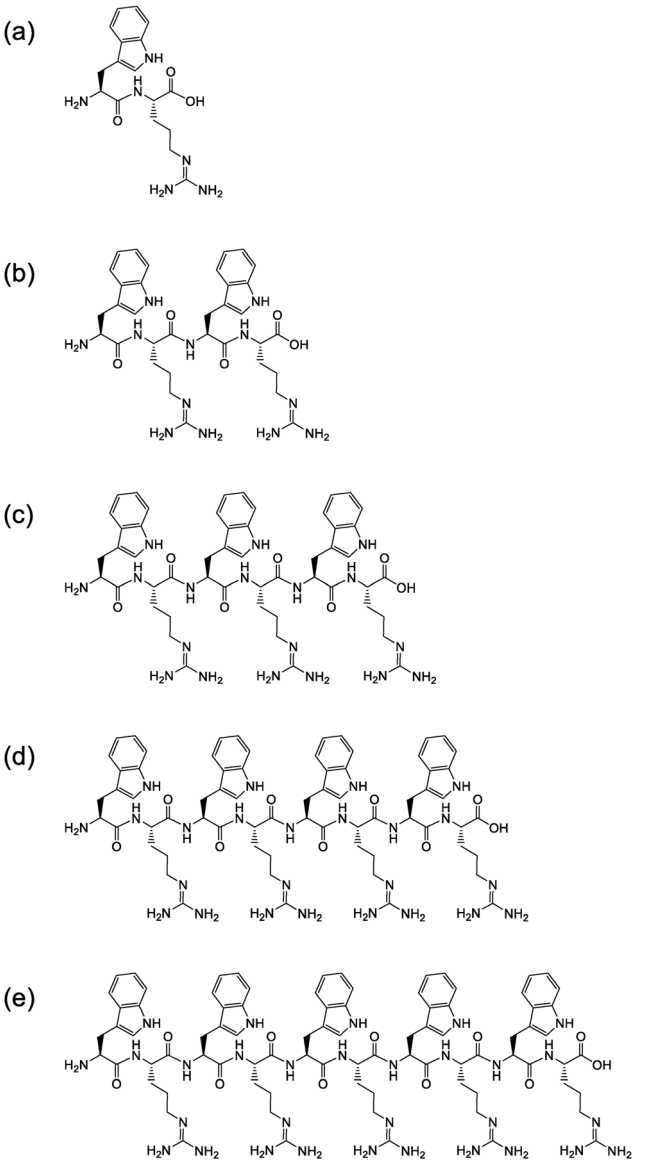

Scheme 1 Molecular structure of $(WR)_n$ with n = (a) 1, (b) 2, (c) 3, (d) 4 and (e) 5.

Materials and methods

Materials

Peptides were obtained from Peptide Synthetics (Peptide Protein Research), Farnham, UK as TFA salts with >95% purity as confirmed by RP-HPLC. Molar masses by ESI-MS are as follows. (WR): 361.2 g mol^{-1} (360.4 g mol^{-1} expected); $(WR)_2$: 704.7 g mol^{-1} (702.8 g mol^{-1} expected); $(WR)_3$: 1047 g mol^{-1} (1045.2 g mol^{-1} expected); $(WR)_4$: 1389.4 g mol^{-1} (1387.6 g mol^{-1} expected); $(WR)_5$: 1732 g mol^{-1} (1730 g mol^{-1} expected). Scheme S1 shows the molecular structures of $(WR)_n$ with n = 1–5.

Sample preparation

Samples of $(WR)_{n=1-5}$ were prepared by mixing weighed amounts of peptide into water or PBS buffer pH 7.4. For titration curves or

samples at pH 12, the pH of the solutions was increased by titrating 0.5–1.4 wt% NaOH into aqueous $(WR)_{n=2-5}$ solutions. The pH of solutions was measured with a Mettler Toledo FiveEasy pH meter with Sigma-Aldrich micro pH combination electrode (glass body). The pH of gels was measured using indicator paper.

A separate set of samples was prepared for confocal microscopy experiments, where an aqueous solution containing rhodamine B (RhoB) was used instead of pure water, to obtain a final 3×10^{-4} wt% RhoB.

Fluorescence microscopy

Thioflavin T (ThT) fluorescence spectra was recorded with a Varian Cary Eclipse fluorescence spectrometer with samples in 4 mm inner width quartz cuvettes. ThT fluorescence assays were conducted using a series of $(WR)_{n=1-5}$ solutions dissolved in 5×10^{-3} wt% ThT. The spectra were recorded from 460 to 600 nm using an excitation wavelength of λ_{ex} = 440 nm.

Circular dichroism (CD) spectroscopy

Far-UV CD spectra were collected using a Chirascan spectropolarimeter (Applied Photophysics, Leatherhead, UK) equipped with a thermal controller. Spectra were recorded from 180 to 400 nm. Samples were mounted in a quartz cell with detachable windows, with 0.01 mm path length. The CD signals from the samples were corrected by water background subtraction. Where necessary, the CD signal was smoothed using the Chirascan software for data analysis. The residual of the calculation was chosen to oscillate around the average, to avoid artifacts in the smoothed curve. CD data, measured in mdeg, was normalized to molar ellipticity using the molar concentration of the sample and the cell path length.

Optical microscopy

Solutions were mounted in quartz cells with detachable windows, with 0.5 mm path length. Images were recorded using an Olympus LmPlanFI 50×/0.5 lens together with a GT Vision GXCAM camera.

Laser scanning confocal microscopy (LSCM)

Imaging was performed using a Nikon A1 HD25/A1R HD25 confocal microscope. Solutions were prepared as detailed in the sample preparation method. Samples were loaded in a well of a microslide 8 well glass bottom plate. Experiments were performed using a Plan Apo λ 100× oil lens. Pinhole sizes were between 20.43 and 72.8 μm. A set of solutions was stained with 3×10^{-4} wt% RhoB, the dye being excited at 561 nm and the emission measured at 595 nm. Another set of solutions was stained with 5×10^{-3} wt% ThT, with ThT excited at 488 nm and the emission measured at 525 nm.

Cryo-scanning electron microscopy (cryo-SEM)

Imaging was performed using a Helios 5 CX DualBeam (Thermo Scientific) FIB-SEM (focused ion beam scanning electron microscope) in high vacuum mode. The samples were mounted between two rivets with each of the bottom rivets held in a slot on an aluminium stub. The stub was then secured on a specimen shuttle which was then plunged into nitrogen slush at approximately −210 °C. Once the samples were frozen the shuttle was retracted and transferred under vacuum to the PP3010T cryo-SEM preparation chamber (Quorum Technologies Ltd) held at −140 °C. To achieve a fractured surface the top rivets were removed with the knife inside the chamber at −190 °C. The temperature inside the chamber was then raised to −90 °C for 10 minutes to sublimate any surface ice then reset to −140 °C to coat the samples with a thin layer of platinum for 30 seconds, prior to imaging at 10 kV (xT Microscope Server version 17.5.0).

Small-angle X-ray scattering experiments (SAXS) and wide angle scattering (WAXS)

SAXS/WAXS experiments were performed on beamline B21[29] at Diamond (Didcot, UK). The sample solutions were loaded into the 96-well plate of an EMBL BioSAXS robot and then injected *via* an automated sample exchanger into a quartz capillary (1.8 mm internal diameter) in the X-ray beam. The quartz capillary was enclosed in a vacuum chamber, to avoid parasitic scattering. After the sample was injected into the capillary and reached the X-ray beam, the flow was stopped during the SAXS data acquisition. To measure very viscous gels, samples were loaded into the multipurpose sample cell holder, specifically designed to measure highly viscous samples and solids at B21.[30] Beamline B21 was operated with a fixed camera length (3.9 m) and fixed energy (12.4 keV). The images were captured using a PILATUS 2 M detector. Data processing was performed using dedicated beamline software ScÅtter.

WAXS measurements were performed on stalks prepared by drying a drop of solution suspended between the ends of wax-coated capillaries. The stalks were loaded into the same cell for viscous samples mentioned above.[30] The WAXS signal was acquired using a Dectris Eiger 2 1M detector, and the q-axis was calibrated using the diffraction spectrum of silver behenate and the intensity normalized using the signal of water. The WAXS data was corrected by background subtraction using the WAXS signal from an empty gel cell.

Fibre XRD

Measurements were performed on the peptide stalks described above for WAXS experiments. The stalks were mounted onto a four axis goniometer of an Oxford Diffraction Gemini Ultra instrument. The sample-detector distance was 44 mm. The X-ray wavelength λ = 1.54 Å was used to calculate the scattering vector $q = 4\pi \sin\theta/\lambda$ (2θ: scattering angle). The detector was a Sapphire CCD.

SAXS and SAXS/WAXS/XRD data analysis

The SAXS data for the samples studied in this work was fitted using a combination of detailed different form factors.

The SAXS data for samples containing $(WR)_2$ was fitted using a combination of the generalized Gaussian coil form factor model (fitting parameters: forward scattering, I_O, radius of gyration, R_g, and Flory exponent ν) to describe the high q scattering[31] and a Porod scattering from discrete objects

$I_S \sim q^{-n}$ (fitting parameters forward scattering I_S and exponent n) to describe low q scattering.

SAXS data for samples containing peptide $(WR)_3$ was fitted using the form factor of a long cylinder (fitting parameters forward scattering, I_C, and cross section radius, $R_C \pm \Delta_{RC}$)[31–33] together with the contribution of a generalized Gaussian coil and a sloping background.

SAXS data for solutions containing peptide $(WR)_4$ was fitted using the contribution to the form factor of a long cylinder, together with a Gaussian bilayer density profile. The bilayer model assumes an electron density profile comprising Gaussians for the headgroups on either side of the bilayer and another Gaussian for the hydrocarbon chain[34] (fitting parameters Gaussian inter-head group thickness and polydispersity, $2z_H \pm \Delta_{2z_H}$; Gaussian half-width for outer layer surface, σ_H; scattering contrast for headgroup, η_H; Gaussian half-width for inner layer; σ_C, scattering contrast for inner layer, η_C). The interactions between bilayers was described using a modified Caillé structure factor, which corresponds to a multilayer structure influenced by thermal fluctuations[31,35] (fitting parameters: number of layers N, lamellar spacing d, Caillé parameter γ).

SAXS data for solutions containing peptide $(WR)_5$ were fitted using a form factor with contributions from a long cylinder and a Gaussian bilayer density profile and Caillé structure factor. The analytical expressions of all the models described above are embedded in the software SASfit,[36,37] used to fit the SAXS data.

SAXS/WAXS/XRD unit cell determination from measured d-spacings was performed using the software CLEARER.[38]

Dynamic light scattering (DLS)

DLS measurements were done using an ALV/CGS-3 Compact Goniometer System with ALV/LSE-5003 correlator using vertical polarized incident light of wavelength 632.8 nm. Measurements were performed at an angle $\theta = 90^\circ$ to the incident beam. The intensity autocorrelations functions were analyzed by the constrained regularized CONTIN method,[39] to obtain distributions of hydrodynamic radius, R_H, of the particle.

Cryogenic-TEM (cryo-TEM)

Imaging was carried out using a field emission cryo-electron microscope (JEOL JEM-3200FSC), operating at 200 kV. Images were taken in bright field mode and using zero loss energy filtering (omega type) with a slit width of 20 eV. Micrographs were recorded using a Gatan Ultrascan 4000 CCD camera. The specimen temperature was maintained at −187 °C during the imaging. Vitrified specimens were prepared using an automated FEI Vitrobot device using Quantifoil 3.5/1 holey carbon copper grids with a hole size of 3.5 μm. Just prior to use, grids were plasma cleaned using a Gatan Solarus 9500 plasma cleaner and then transferred into the environmental chamber of a FEI Vitrobot at room temperature and 100% humidity. Thereafter 3 μL of sample solution was applied on the grid and it was blotted twice for 5 seconds and then vitrified in a 1/1 mixture of liquid ethane and propane at temperature of −180 °C. The grids with vitrified sample solution were maintained at liquid nitrogen temperature and then cryo-transferred to the microscope.

Cell viability assays by MTT

Reagents: human dermal fibroblasts from adult donors (HDFa) cells and 3-(4,5-dimethylthiazol-2-yl)-2,5-diphenyltetrazolium bromide (MTT) were purchased from Merck SigmaAldrich (Gillingham, UK). DMEM/F12 and fetal bovine Serum (FBS) were obtained from ThermoFisher (UK) and DMSO from Fisher Scientific (UK). Protocol: to evaluate the cytocompatibility of the sequences presented in this work, HDFa cells were cultivated in DMEM/F12 supplemented with 5% of FBS until reaching confluence. The cells were maintained inside a cell incubator at 37 °C and a CO_2 atmosphere of 5%. Then, cells were harvested and seeed in 96 well plates, with a cell density of 5×10^3 per well at a final volume of a 100 μL and left to attach for 24 hours inside a cell incubator. On the next day, the plates were washed three times with PBS and different concentrations of peptides were diluted in DMEM/F12 and added to the wells containing HDFa cells. The controls were incubated only in DMEM/F12. All wells contained a final volume of 100 μL. The plates were then incubated for 72 hours inside a cell incubator at 37 °C with a CO_2 atmosphere of 5% and again washed three times with PBS after 3 days incubation. After washing with PBS, the cells were incubated in a 100 μL of media containing 0.5 mg mL^{-1} of MTT and again incubated for 5 hours, protected from the light. To solubilize the resulting formazan crystal, 100 μL of DMSO was added to each well and incubated at 37 °C

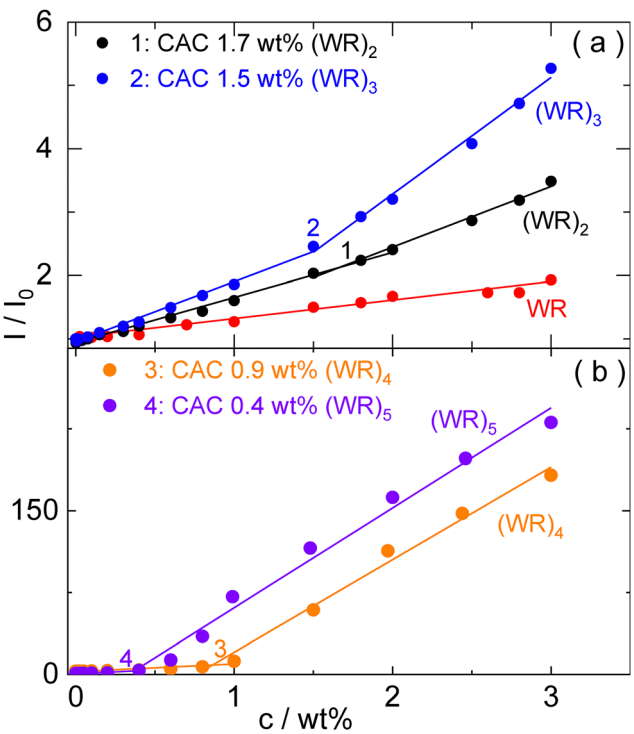

Fig. 1 ThT curves and CAC values for (a) $(WR)_{n=1-3}$, (b) $(WR)_{n=4,5}$ in native solutions. Data for $(WR)_4$ has been multiplied by 3.5, for ease of visualization.

for 45 minutes wrapped in aluminium foil to prevent photo-degradation. The resulting absorbance was read at 560 nm using a Tecan Infinite F50 instrument (Männedorf, Switzerland).

Results

To examine β-sheet formation for the $(WR)_{n=1-5}$ peptides (Scheme S1) Thioflavin T (ThT) fluorescence assays were performed in native solutions at pH 2.5. The dye probe ThT binds to β-sheet 'amyloid' structures,[40,41] the building blocks of peptide fibres. The fluorescence emission intensity was recorded for ThT-peptide solutions (I) or the pure ThT solution (I_0). Fig. 1 shows plots of I/I_0 against peptide concentration, which allows the critical aggregation concentration (CAC) for peptide fibril formation to be determined from a discontinuity in each curve. The data indicate that WR does not self-assemble into β-sheet structures in solution (Fig. 1a), while $(WR)_{n=2-5}$ form fibres in aqueous solutions at concentrations above CAC values 1.7, 1.5, 0.9 and 0.4 wt% peptide for $(WR)_2$, $(WR)_3$, $(WR)_4$ and $(WR)_5$ respectively. The decrease in CAC with increasing sequence length is consistent with increased peptide aggregation propensity.

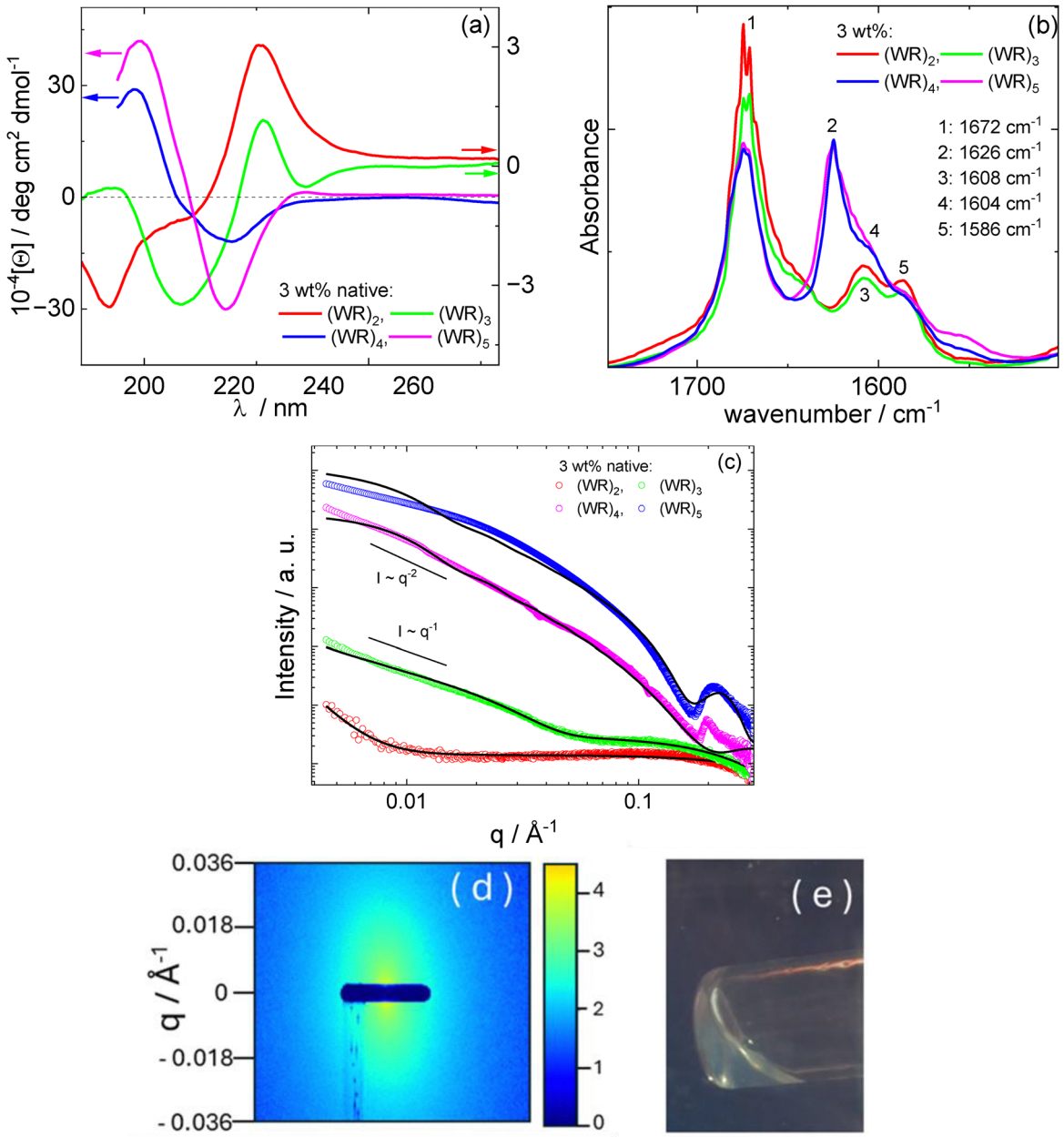

Fig. 2 (a) CD, (b) FTIR and (c) and (d) SAXS data for 3 wt% $(WR)_{n=1-5}$ at native pH = 2.5 The full lines in (c) are the fitting of the SAXS data as described in the manuscript. SAXS curves for $(WR)_4$ and $(WR)_5$ in (c) are multiplied by 4 and 16.7 respectively, for ease of visualization. Data for 3 wt% $(WR)_4$ in water: (d) 2D SAXS pattern showing orientation along the flow direction in the capillary and (e) birefringence of the sample observed through crossed polarizers.

We previously reported that LLPS, one focus of this work, does not occur in WR basic solutions.[28] Therefore, in the following, WR serves as a useful non-assembling peptide reference.

Titration curves following addition of a NaOH solution were measured for $(WR)_{n=2-5}$ to confirm pK_a values for the peptides in solution. The titration curves displayed in SI Fig. S1 start from a 1 wt% $(WR)_{n=2-5}$ solution in pure water with pH $\sim$ 2.5 for all the native solutions. The software HYSS[42] was used to calculate the theoretical titration curves (pK_a(1) = 12.5 for R, pK_a(2) = 7 for the N-terminus and pK_a(3) = 3.5 for the C-terminus[28]) and these are plotted along with the experimental results in SI Fig. S1. The assumed pK_a values lead to good agreement between experimental and theoretical titration curves. It is noted that pH 7.4 corresponds to the physiological condition and sets the reference for biological assays reported below, while we previously reported LPPS in W_2R_2 and W_3R_3 solutions at pH 12.[28] Based on these facts, it is reasonable to constrain our study to the self-assembly of $(WR)_{n=2-5}$ in water (native pH = 2.5), solutions at pH 7.4 or solutions at pH 12. In the following, pH 7.4 will be adjusted using PBS buffer, to more closely match to biological conditions, while pH 12 will be attained by titrating a NaOH solution, to match the conditions used in our previous work.[28] At native pH the arginine residues and termini are expected to all be charged. The pH 7.4 is close to the pK_a of the N-terminus (leading to reduction by up to +1 of the cationic charge) whereas pH 12 is close to the pK_a of arginine, so these residues would expect to be not fully charged.[28] A combination of CD, FTIR and XRD, were used to probe peptide conformation together with cryo-TEM and SAXS to determine self-assembled motifs and associated dimensions. Fig. 2 shows CD, FTIR and SAXS data measured for $(WR)_{n=2-5}$ native solutions at pH 2.5. The CD spectrum for 3 wt% $(WR)_2$ (Fig. 2a) is dominated by a minimum at 192 nm and a maximum at 226 nm. A similar maximum is present for 3 wt% $(WR)_3$ but the minimum is displaced to 208 nm. The CD peak at 226 nm is assigned to electronic transitions of the W residue.[28,43,44] The minimum at 192–208 nm corresponds to a disordered structure.[28,45–48] However, for $(WR)_3$, the minimum is shifted towards higher wavelength due to a β-sheet contribution to the signal. In contrast, CD spectra for both 3 wt% $(WR)_4$ and $(WR)_5$ present a maximum at 198 nm and a minimum at 218 nm, corresponding to a β-sheet secondary structure (Fig. 2a).[49]

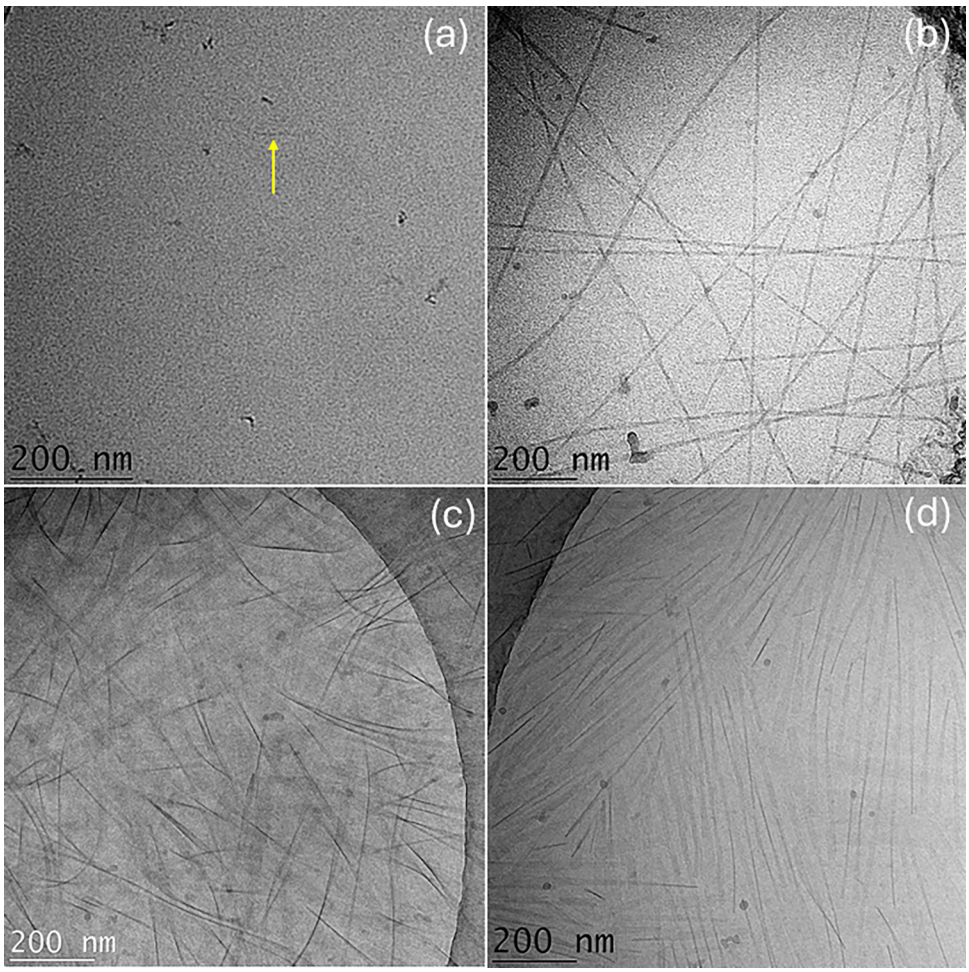

Fig. 3 Cryo-TEM images at native pH = 2.5 for 3 wt% $(WR)_n$; n = (a) 2, (b) 3 and (d) 5. (c) 3 wt% native $(WR)_4$ diluted to 1 wt% just before the experiment, to improve grid preparation. The arrow in (a) points to an isolated fibril in the solution.

FTIR spectra show a speak at 1672 cm^{-1} for 3 wt% $(WR)_{n=2-5}$, due to TFA counterions bound to the arginine residue (Fig. 2b).[50–52] Stretching deformations of the arginine side chain give rise to the bands at 1604–1608 cm^{-1} and 1586 cm^{-1} for $(WR)_{n=2-4}$,[53,54] while a peak at 1626 cm^{-1} denotes a β-sheet secondary structure for $(WR)_{n=4-5}$.[49,55] SAXS (Fig. 2c) reveals form factor features. The data was fitted using the models described in the Experimental section. The parameters obtained from the fitting to the SAXS data are listed in SI Table S1. The SAXS data for 3 wt% $(WR)_2$ has features of unaggregated peptide monomers and was fitted to a generalized Gaussian coil together with a sloping background. In contrast, the data for longer sequences $(WR)_{n=3-5}$ shows form factor features associated with extended self-assembled structures. A long cylinder form factor was used to fit the SAXS data for 3 wt% $(WR)_3$, consistent with intensity scaling at low wavenumber q, $I \sim q^{-1}$ (Fig. 2c).[31] In contrast, the data for $(WR)_4$ and $(WR)_5$ show a scaling $I \sim q^{-2}$, consistent with layer structures, and the shape of the form factor at high q is also quite different from that for $(WR)_3$. A bilayer form factor was used to fit the SAXS data of $(WR)_4$, while this form factor together with contribution from long cylinders and a sloping background was used to fit the SAXS data for $(WR)_5$. The SAXS data in Fig. 2c indicates that the formation of extended structures (fibrils or bilayer nanotapes) increases with the number of WR repeats. These findings are consistent with the CD and FTIR spectra which show β-sheet structure develops, especially for $(WR)_4$ and $(WR)_5$. The bilayer thickness from the SAXS fits can be compared to the length of the peptides in an extended β-sheet configuration which are 27.2 or 34.0 Å for $(WR)_n$ with n = 4 or 5 respectively, assuming a 3.4 Å length per extended residue in an antiparallel β-sheet. This is consistent with the bilayer thickness of ~30 Å obtained from the SAXS fitting (SI Table S1). This result was confirmed by the data for 3 wt% $(WR)_4$ which shows a sharp Bragg-like peak corresponding to a bilayer spacing of 31.4 Å (Fig. 2c). The 2D SAXS pattern for 3 wt% $(WR)_4$ displayed an oriented pattern (Fig. 2d) while the sample was birefringent (Fig. 2e), suggesting the formation of nematic ordering. It has previously been noted that the related peptide $(RF)_4$ shows an anisotropic SAXS pattern.[25]

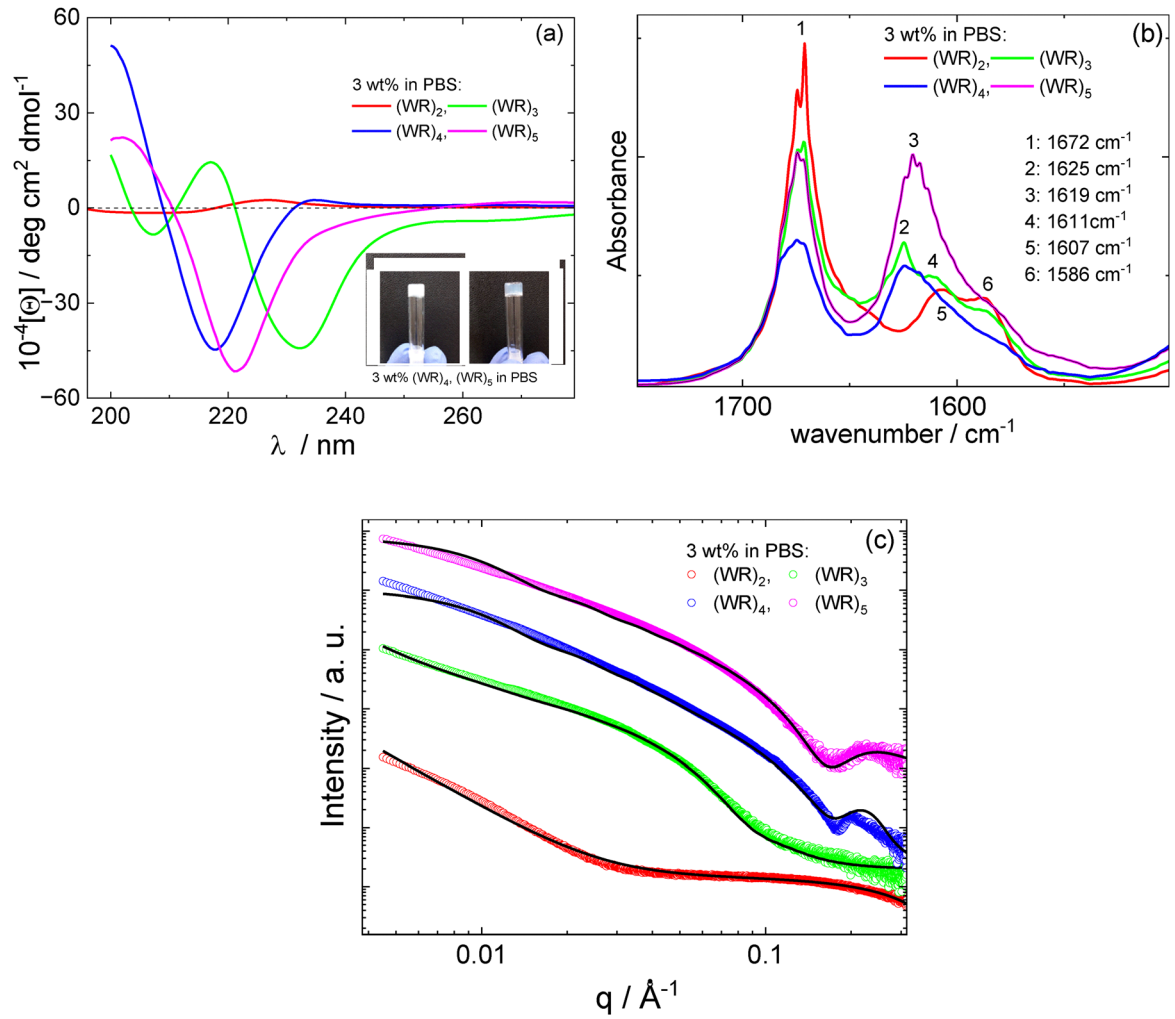

Fig. 4 (a) CD, (b) FTIR and (c) SAXS data for 3 wt% $(WR)_{n=2-5}$ in PBS. The full lines in (c) are the fitting of the SAXS data as described in the manuscript. SAXS curves for $(WR)_3$, $(WR)_4$ and $(WR)_5$ in (c) are multiplied by 10, 40 and 100 respectively, for ease of visualization.

To further examine self-assembled nanostructures, SAXS was complemented with cryo-TEM. Fig. 3 shows the cryo-TEM images for 3 wt% $(WR)_{n=2-5}$ at native pH = 2.5. The cryo-TEM image for $(WR)_2$ (Fig. 3a) shows predominantly micelle-like structures along with a small population of fibrils. In contrast, the image for $(WR)_3$ (Fig. 3b), is dominated by long twisted peptide fibrils of ~15 nm width (some micelle-like structures can also be discerned). The cryo-TEM image for $(WR)_4$ reveals the presence of ~30 nm wide twisted nanotapes (Fig. 3c). The formation of ~20 nm wide tapes can be observed for $(WR)_5$ in water (Fig. 3d); some of them presenting 6 nm wide stripes (SI Fig. S2). The cryo-TEM images in Fig. 3 are consistent with the SAXS data in Fig. 2c for $(WR)_n$ with n = 3–5 showing fibrillar or bilayer nanotape structures, although possibly due to low core–shell contrast (or low population relative to monomers) the micellar form factor for $(WR)_2$ was not detected.

Having studied solutions at native pH 2.5, we then examined conformation and self-assembly in physiologically relevant conditions using PBS pH 7.4. Fig. 4 shows the CD (Fig. 4a), FTIR (Fig. 4b) and SAXS (Fig. 4c) data for $(WR)_{n=2-5}$ in PBS above each CAC (data in Fig. 1). The images inset in Fig. 4a highlight that 3 wt% $(WR)_{n=4-5}$ samples in PBS pH 7.4 are hydrogels since the samples do not flow upon tube inversion. The CD spectrum shown in Fig. 4a for $(WR)_2$ is dominated by a minimum at 208 (from disordered structure) and a maximum at 226 nm (from absorption of the W residue). The CD spectrum for 3 wt% $(WR)_3$ indicates a coexistence of disordered structure (minimum at 207 nm) together with a β-sheet secondary structure (maximum and minimum at 216 and 232 nm respectively). The minima at 218–220 nm for 3 wt% $(WR)_{n=4-5}$ denote a β-sheet secondary structure.[45,56,57] FTIR spectra (Fig. 4b) contain a peak at 1672 cm^{-1} for 3 wt% $(WR)_{n=2-5}$, due to TFA counterions bound to the arginine residues, as mentioned above. Arginine side chain stretching modes give rise to the bands at 1607–1611 and 1586 cm^{-1} for $(WR)_{n=2-3}$,[53,54] while peaks at 1619 and 1625 cm^{-1} are signatures of β-sheet secondary structure for $(WR)_{n=3-5}$.

The CD and FTIR spectra in Fig. 4a and b, show that using PBS as a solvent for $(WR)_n$ leads to clearer signals of β-sheet formation starting at n = 3 as opposed to n = 4 for native solutions (Fig. 2a and b). Fig. 4c shows SAXS data measured for $(WR)_{n=2-5}$ in PBS. The parameters used to fit the data are listed in SI Table S2. For each peptide, the model used to fit the SAXS data in PBS is the same used to fit the SAXS data in water. As discussed above, the self-assembly evolves from a disordered

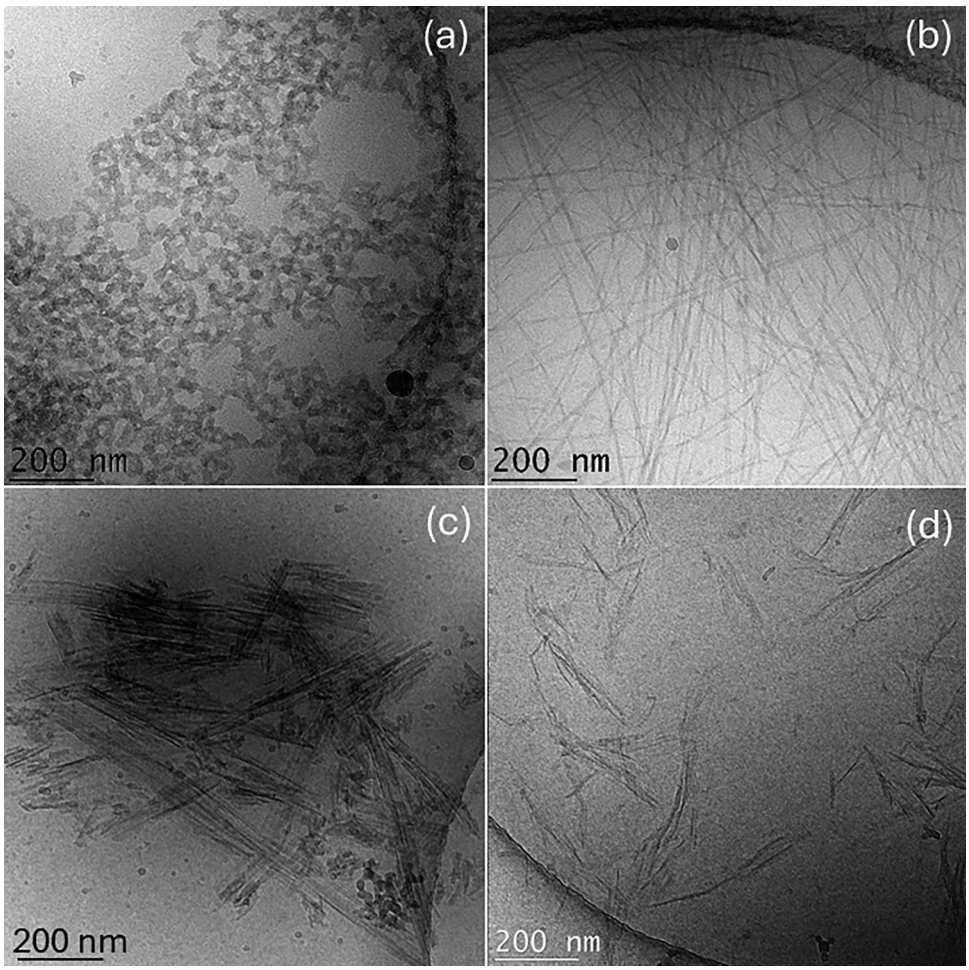

Fig. 5 Cryo-TEM images measured for 3 wt% $(WR)_n$ PBS solutions; (a) n = 2 and (b) n = 3. Cryo-TEM images measured for 2 wt% $(WR)_n$ PBS soft gels; (c) n = 4 and (d) n = 5. 2 wt% soft gels were diluted to 1 wt% just before the experiment, to improve grid preparation.

Table 1 *d*-Spacings measured from SAXS/WAXS and XRD data in SI Fig S5, together with unit cell indexation assuming an orthorhombic cell

3 wt% $(WR)_3$ PBS			3 wt% $(WR)_4$ PBS			3 wt% $(WR)_5$ PBS		
	d spacings [Å]			*d* spacings [Å]			*d* spacings [Å]	
h k l	Calc.	Exp.	*h k l*	Calc.	Exp.	*h k l*	Calc.	Exp.
0 −1 0	28.27	27.87	0 1 0	30.26	31.55	1 0 0	31.92	32
−1 0 0	19.98	19.62	2 0 0	15.13	15.01	2 0 0	15.96	16.08
0 −2 0	14.13	13.71	2 1 0	10.56	10.73	0 0 1	9.6	11.03
−1 0 −1	8.73	9.1	0 1 1	8.04	8	0 2 0	7.52	7.55
0 2 −1	7.99	8.188	3 1 1	6.29	6.34	3 1 1	6.44	6.49
3 1 0	6.48	6.353	2 2 1	5.45	5.44	4 2 0	5.473	5.47
3 0 1	5.49	5.42	1 0 2	4.74	4.76	4 2 1	4.75	4.77
0 0 2	4.85	4.77	3 3 0	4.42	4.4	1 3 1	4.4	4.41
0 2 −2	4.59	4.58	4 1 2	3.9	3.91	4 1 2	3.97	3.95
0 3 −2	4.31	4.29	3 2 2	3.74	3.73	1 4 0	3.73	3.72
3 0 −2	3.92	3.95	0 0 3	3.2	3.2	3 5 2	2.49	2.48
3 2 −2	3.78	3.8	2 5 2	2.48	2.48	—	—	—
—	—	—	3 4 3	2.35	2.35	—	—	—
Unit cell calculation and average error								
a = 19.9 Å, b = 28.3 Å, c = 9.7 Å			a = 30.3 Å, b = 14.7 Å, c = 9.6 Å			a = 31.9 Å, b = 15.0 Å, c = 9.6 Å		
ε = 0.05%			ε = 0.004%			ε = 0.14%		
Molecule length[a]								
20.4 Å			27.2 Å			34 Å		

[a] Calculated assuming 3.4 Å per residue in an extended β-sheet configuration.

structure towards a self-assembled tape upon increasing the number of repeat $(WR)_n$ units from n = 2 to 5, the first features of fibril formation appearing for $(WR)_3$ in agreement with CD and FTIR results (Fig. 4a and b). However, 3 wt% samples of

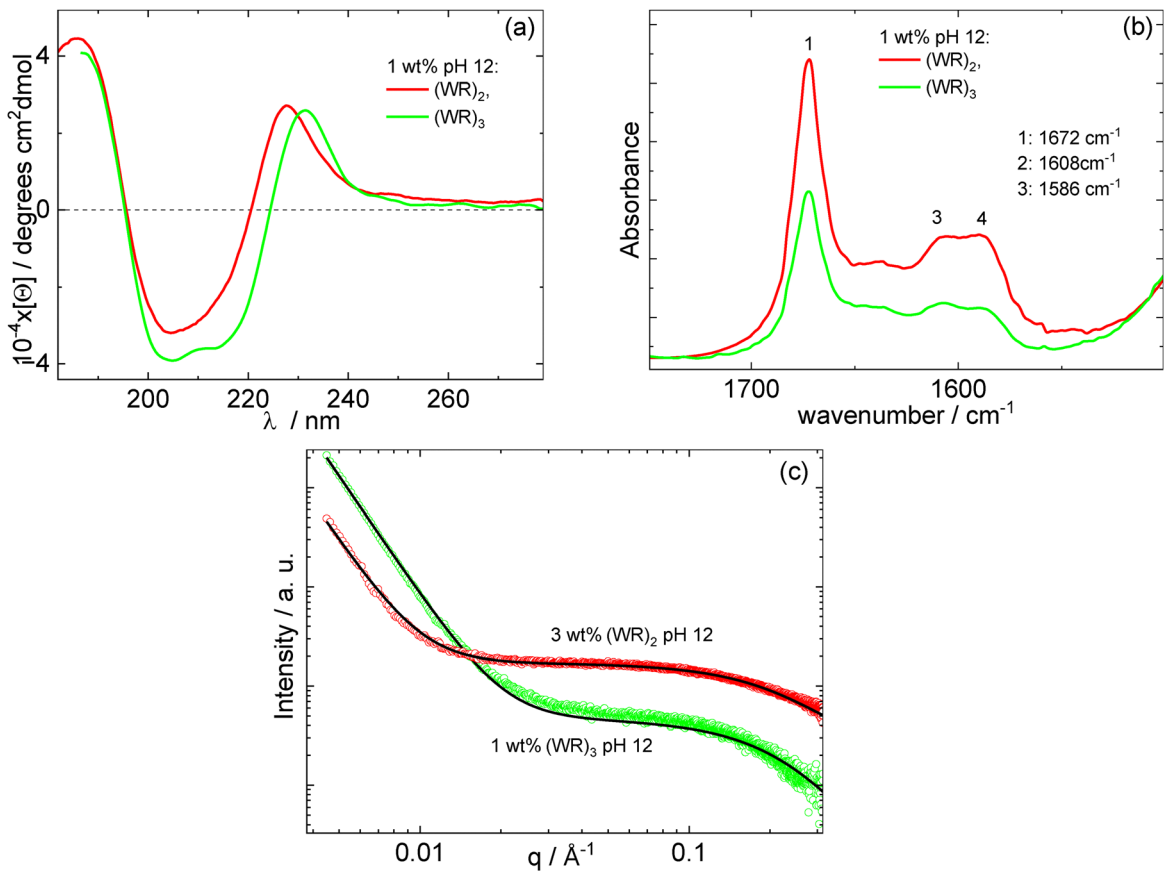

Fig. 6 (a) CD, (b) FTIR and (c) SAXS data for 1 or 3 wt% $(WR)_{n=2-3}$ at pH 12. The solid lines in (c) are the fitting of the SAXS data as described in the manuscript. To reduce noise in the data, SAXS data was measured at 3 wt% for $(WR)_2$.

$(WR)_{n=4-5}$ are gels (Fig. 4a) in contrast to the solutions at native pH. The SAXS data for $(WR)_2$ shows features at higher q corresponding to monomers with an upturn in the intensity at low q (described in the fit by a power law function) that can be ascribed to globular aggregates, possibly coacervate structures as revealed by cryo-TEM discussed below.

Cryo-TEM images to complement SAXS and for comparison with images obtained at native pH (Fig. 3) for 3 wt% $(WR)_{n=2-3}$ solutions and 2 wt% $(WR)_{n=4-5}$ soft gels in PBS are displayed in Fig. 5 and SI Fig. S3. Cryo-TEM images show a globular network for $(WR)_2$ (Fig. 5a), assembled from individual globules ~20 nm in diameter (SI Fig. S3). Long tapes ~15 nm thick are observed for $(WR)_3$ (Fig. 5b), some of them twisted into ~7 Å thick rods. A co-existence of globular structures ~20 nm in diameter with up to ~70 nm thick tapes comprising ~10 nm stripes is observed for $(WR)_4$ (Fig. 5c), whereas $(WR)_5$ shows the coexistence of extended and twisted tapes up to ~30 nm thick (Fig. 5d). Peptide $(WR)_4$ forms a hard gel at 3 wt% in PBS and this was imaged using cryo-SEM (SI Fig. S4); images show wide tapes, with ~15 nm thick stripes, together with polydisperse globular objects up to ~35 nm in diameter. This structure agrees with that revealed in cryo-TEM images for the soft gel formed by 2 wt% $(WR)_4$ in PBS (Fig. 5c).

Additional information can be obtained by considering SAXS results (Fig. 4c) along with cryo-TEM and cryo-SEM images. SAXS did not detect the overall shape of the globular aggregates revealed by cryo-TEM for $(WR)_{n=3-4}$ because the scattering is dominated by the contribution from fibres or bilayers in the solution, while the SAXS signal for $(WR)_2$ results from the phase separation between dense regions of peptide and solvent. SAXS suggests that the globular aggregates revealed by cryo-TEM do not have an internal structure but may result from peptide self-coacervation in PBS.

The spectroscopic data show that nanotapes and fibres self-assembled in PBS (revealed by SAXS and electron microscopy) present a β-sheet secondary structure. SAXS/WAXS and XRD spectra were measured for fibres dried from a 3 wt% PBS $(WR)_3$ solution or 3 wt% PBS $(WR)_{n=4-5}$ gels to study the packing of the molecules in the β-sheets. The peak positions in the X-ray data, displayed in SI Fig. S5, were used to determine a set of d-spacings. The indexation of these d-spacings, assuming an orthorhombic cubic cell, is shown in Table 1. The peptides are extended along the a-axis of the unit cell (Table 1). The dimensions a = 19.9, 30.3 Å and 31.9 Å measured for $(WR)_3$, $(WR)_4$ and $(WR)_5$ respectively are close to the extended length of the molecules $(WR)_3$ = 20.4 Å, $(WR)_4$ = 27.2 Å and $(WR)_5$ = 34 Å (Table 1). The c-axis length ~9.6 Å (Table 1) corresponds to twice the β-strand spacing in a β-sheet configuration.[58,59]

Having examined conformation and self-assembly at native pH = 2.5 and in PBS at pH 7.4, we also studied aggregation at pH 12 where the molecules are expected to have significantly lower charge as this pH value is above the N-terminal pK_a and

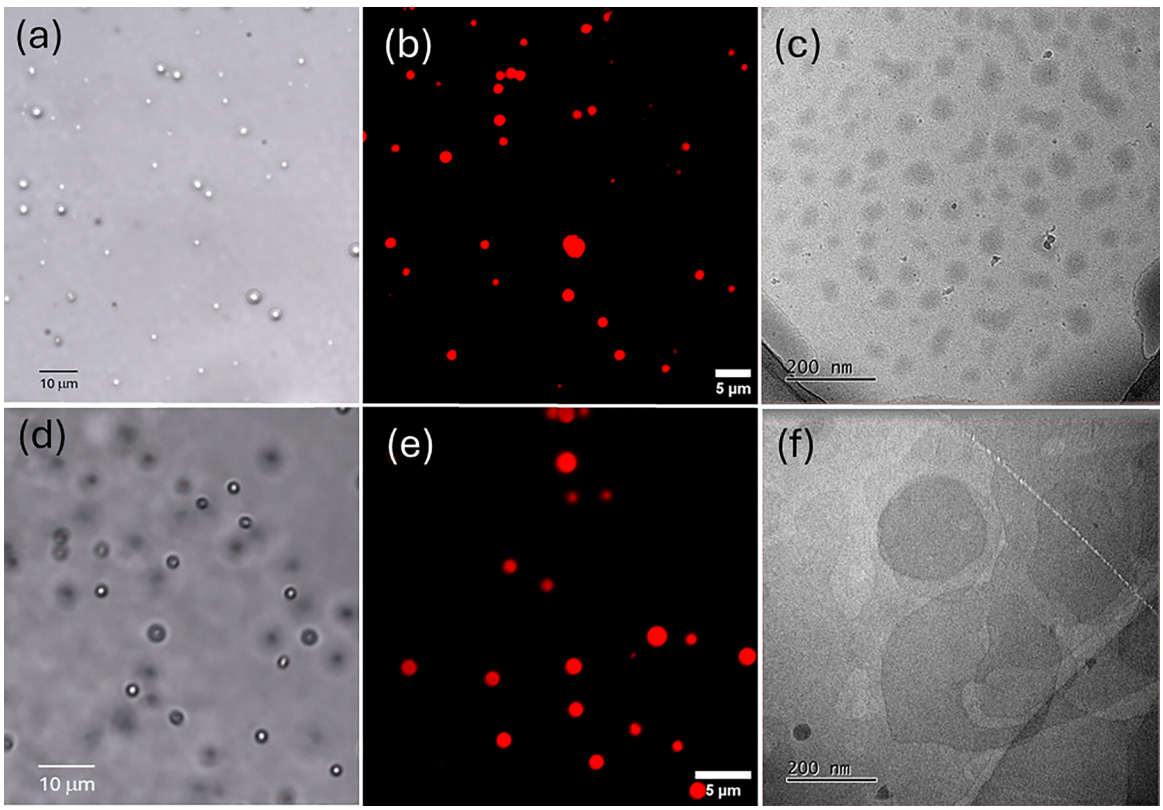

Fig. 7 LLPS characterized by coacervate droplets for 1 wt% $(WR)_2$ at pH 12: (a) optical microscopy, (b) LSCM and (c) cryo-TEM images. Images for 1 wt% $(WR)_3$ pH 12 coacervate droplets: (d) optical microscopy, (e) LSCM and (f) cryo-TEM images. In the cryo-TEM images, droplets are irregular dark objects; in (f) they co-exist with fibres. Samples in (b) and (e) are stained with 3×10^{-4} wt% RhoB.

close to the arginine side-chain pK_a. As discussed below, we found that while $(WR)_{n=2-3}$ undergo self-coacervation (liquid–liquid phase separation, LLPS) at pH 12, $(WR)_{n=4-5}$ self-assemble into fibres at pH 12. Because these are two intrinsically different processes, we will first present results for $(WR)_{n=2-3}$ at pH 12, and then discuss the behaviour of $(WR)_{n=4-5}$ at pH 12. Fig. 6 shows the CD, FTIR and the SAXS data measured for $(WR)_{n=2-3}$ solutions at pH 12. CD data for 1 wt% $(WR)_{n=2-3}$ pH 12 (Fig. 6a) show a positive maximum at ~227 nm for $(WR)_2$ (shifted to 232 nm for $(WR)_3$) together with a secondary shoulder minimum at 214 nm (only for $(WR)_3$), which are due to the absorbance of the W residue. A peak at ~204 nm denotes a disordered structure for both peptides. In contrast to W_2R_2 or W_3R_3 coacervate solutions previously studied by us[28] the CD data in Fig. 6a does not show a large negative peak at 223 nm, from cation–π interactions involving W residues. In fact, the overall features of the CD data in Fig. 6a are similar to those measured for the corresponding native pH solutions (Fig. 2a). FTIR data for 1 wt% $(WR)_{n=2-3}$ pH 12 (Fig. 6b) in the amide I′ region shows a peak at 1672 cm^{-1} due to TFA counterions bound to the arginine residue, while the arginine side chain deformation modes give rise to the bands at 1608 and 1586 cm^{-1}. The SAXS data for 3 wt% $(WR)_2$ or 1 wt% $(WR)_3$ pH 12 solutions are presented in Fig. 6c, including solid lines from form factor fitting. The concentration was increased to 3 wt% for $(WR)_2$ to improve the SAXS contrast. Following our previous study on W_2R_2 and W_3R_3 coacervates,[28] this SAXS data for was fitted using a combination of a generalized Gaussian form factor model (representing monomers in solution) and Porod power-law scattering at low q, arising from irregular aggregates. The parameters extracted from the SAXS fittings are listed in SI Table S3. From the generalized Gaussian coil contribution from monomers, the fitting shows a Flory coefficient $\nu = 0.33$ from compact peptide chains,[60–62] associated to an increase in localized peptide density, a condition for droplet stability. The Porod coefficient is $n = 4$ (*i.e.* intensity scaling $I \sim q^{-4}$ at low q) which describes a discrete object (coacervate droplets).

Optical microscopy, LSCM and cryo-TEM was used to investigate the structure within 1 wt% $(WR)_{n=2-3}$ pH 12 solutions. The images displayed in Fig. 7 and SI Fig. S6, S7 reveal the self-coacervation of $(WR)_{n=2-3}$ at pH 12 into droplets with a wide distribution of sizes. Coacervate droplet sizes for 1 wt% $(WR)_2$ at pH 12 were ~2 μm and (1.4 ± 0.7) μm as measured by optical microscopy (Fig. 7a) and LSCM (Fig. 7b and SI Fig. S6). Cryo-TEM (Fig. 7c) revealed a population of smaller droplets (56 ± 14) nm in diameter. Droplet diameters for 1 wt% $(WR)_3$ pH 12 were ~1.4 μm, (1.3 ± 0.3) μm as measured by optical

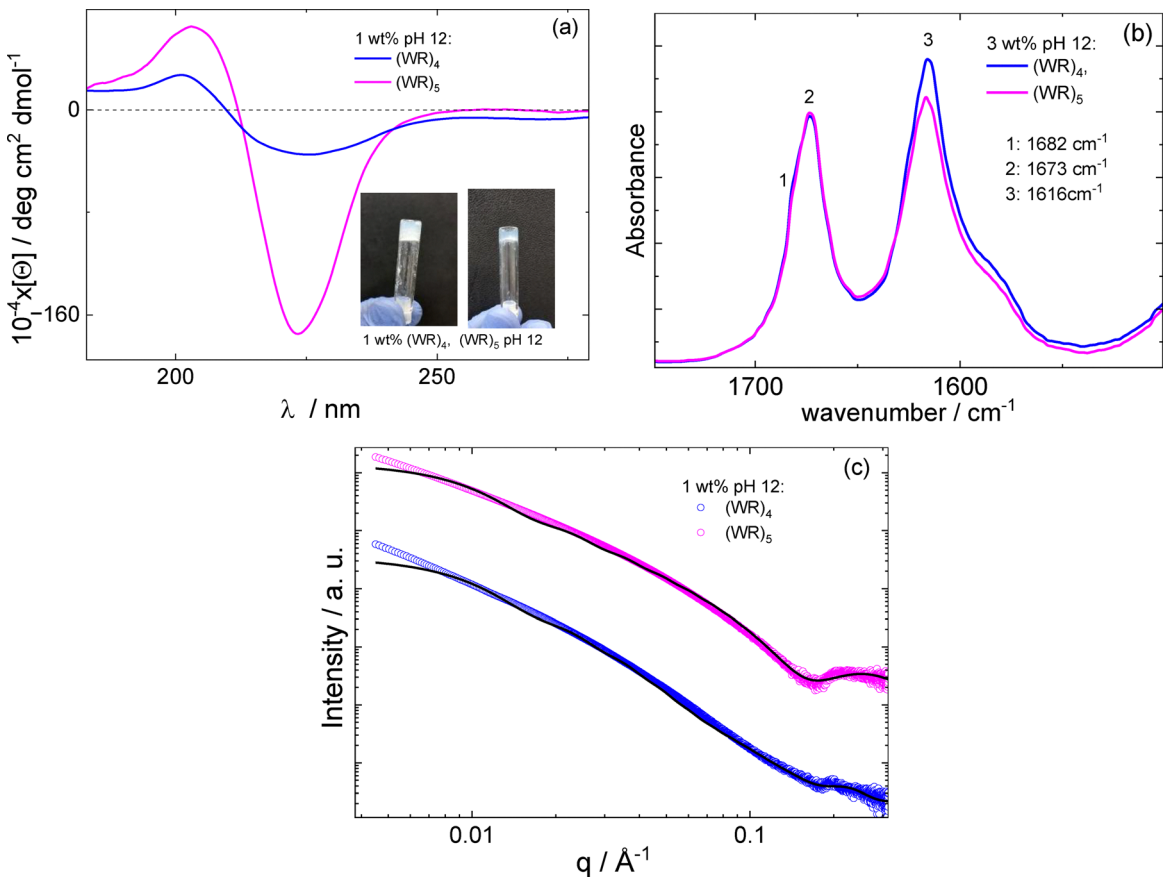

Fig. 8 (a) CD, (b) FTIR and (c) SAXS data for 1 wt% $(WR)_{n=4-5}$ pH 12. The full lines in (c) are the fitting of the SAXS data as described in the manuscript. SAXS curve for $(WR)_5$ in (c) is multiplied by 70, to enable the visualization of the data.

microscopy (Fig. 7d) and LSCM (Fig. 7e and SI Fig. S7) respectively, while cryo-TEM images displayed very polydisperse droplets (80–400) nm in size (Fig. 7f).

Dynamic light scattering (DLS) was used to obtain further information on coacervate droplet sizes for 1 wt% $(WR)_2$ at pH 12. The calculated hydrodynamic radius (R_H) distribution (SI Fig. S8) shows that $(WR)_2$ coacervate size polydispersity is lower than that reported before by us for W_2R_2 coacervates.[28] The average hydrodynamic radius, R_H = 291 nm, measured 10 mins after sample preparation, increases to R_H = 436 nm 1 h after sample preparation and remains nearly stable for the next 24 h (SI Fig. S8).

We explored the formation of hydrogels containing coacervate droplets. Experiments were unsuccessful for $(WR)_2$, but we obtained a hydrogel for 3.5 wt% $(WR)_3$ pH 12 as shown by the inset in SI Fig. S9a showing a sample in an inverted tube. The CD data for the $(WR)_3$ gel (SI Fig S9a) corresponds to β-sheet secondary structure and is dominated by a minimum at 220 nm and a maximum at 193 nm. An additional maximum at 247 nm results from a contribution from electronic transitions of the W residue, possibly red-shifted due to light scattering (the sample shows some cloudiness as in the inset image). The increase in concentration may also cause a red-shift in the characteristic tryptophan aromatic group CD features.[44] The SAXS data for the hydrogel (SI Fig. S9b) was fitted using the form factor for a long cylinder with radius R_C = (1.4 ± 0.9 Å) (SI Table S3). Cryo-SEM images (SI Fig. S9c and d) show that the hydrogel is composed of coacervate droplets, ~200 nm in diameter and fibres ~50 nm thick. This nanostructure is a denser version of that observed for the liquid 1 wt% $(WR)_3$ pH 12 solutions (Fig. 7f). Peptide fibres in cryo-SEM images appear wider than the thickness values obtained from the SAXS data (SI Table S3), because it is likely that the cryo-TEM sample preparation process created bundles of fibres.

Although 1 wt% $(WR)_{n=2-3}$ pH 12 were liquid samples, with a structure defined by the peptide coacervation, we found that 1 wt% $(WR)_{n=4-5}$ pH 12 were hydrogels, consisting of peptide fibres or tapes networks. Fig. 8 shows the CD, FTIR and SAXS data for these samples. The inset in Fig. 8a shows that these samples are hydrogels. The CD data (Fig. 8a), with a maximum at ~200 nm and a minimum at ~224 nm, can be assigned to a β-sheet secondary structure. The amide I' FTIR data for 1 wt% $(WR)_{n=4-5}$ pH 12 (Fig. 8b) presents a peak at 1673 cm^{-1}, due to TFA counterions bound to the arginine residue. A peak at 1616 cm^{-1} from β-sheet secondary structure, along with the shoulder peak at 1682 cm^{-1} suggests an antiparallel β-sheet arrangement, which is expected based on packing considerations and consistent with the modelling of SAXS/WAXS/XRD data (Table 1). Fig. 8c shows the SAXS data measured for 1 wt% $(WR)_{n=4-5}$ at pH 12. The parameters used to fit the data are listed in SI Table S3. For each peptide, the model used to fit the SAXS data at pH 12 is the same used to fit the SAXS data in water or PBS pH 7.4. The SAXS data for 1 wt% $(WR)_{n=4-5}$ pH 12 was fitted to a Gaussian bilayer form factor (Fig. 8c and SI Table S3). The bilayer thickness, in the range 1.8–2.0 nm, is similar to that measured in PBS pH 7.4 (SI Table S2) but notably

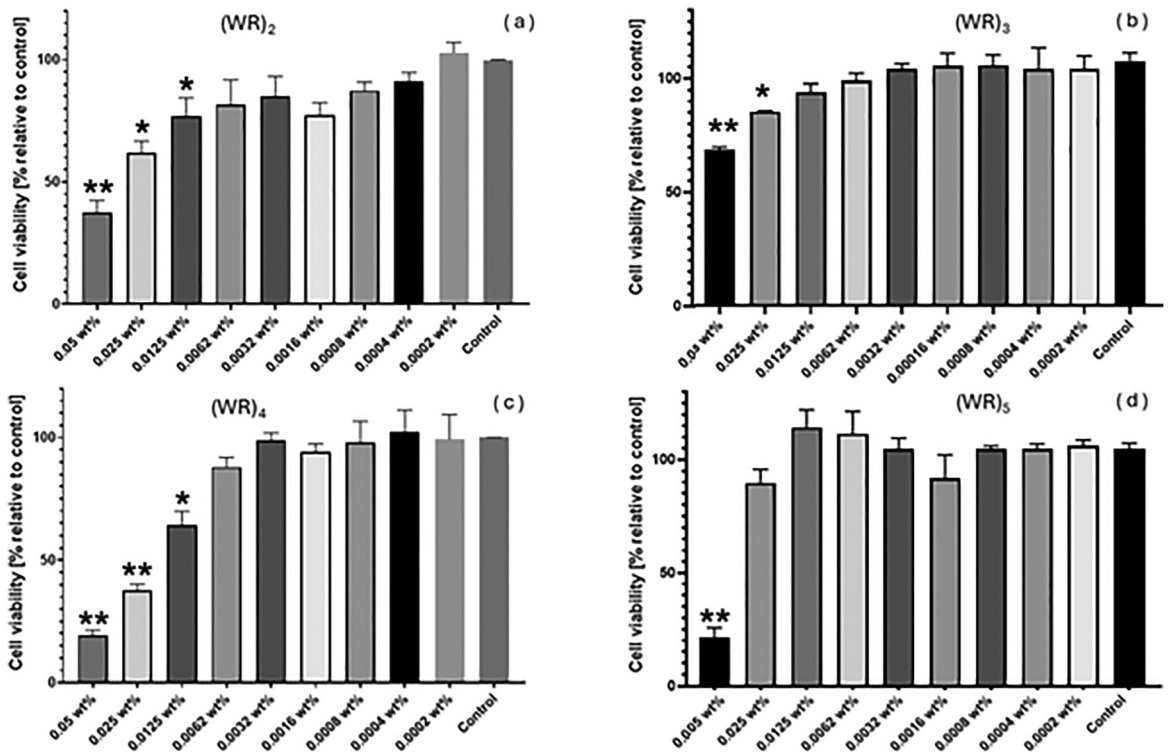

Fig. 9 Cytocompatibility studies using MTT assays. (a) $(WR)_2$, (b) $(WR)_3$, (c) $(WR)_4$ and (d) $(WR)_5$. The statistical analysis was performed by Welch ANOVA, n = 3 and Dunnet correction for multiple comparisons. * Indicates $p \leq 0.05$. ** Indicates $p \leq 0.01$.

smaller than the thickness 3.0 nm measured at native pH 2.5 (SI Table S1). Cryo-SEM images for a 1 wt% $(WR)_4$ pH 12 gel (SI Fig. S10) reveal a network of ~250 Å thick tapes, in good agreement with the fitting of the SAXS data using a bilayer form factor (Fig. 8c and SI Table S3). We found no evidence of coacervation for 3 wt% $(WR)_{n=4-5}$ at pH 12.

The cytocompatibility of all five sequences was determined using MTT assays, which are colorimetric measurements based on reduction of tetrazolium salts inside the cells, especially mitochondria, resulting in insoluble formazan crystals that can be solubilized with the help of organic solvents and indicate the overall metabolism of a cell population.[63,64] As shown in Fig. 9, all sequences were tolerated by fibroblasts for concentrations of 0.0062 wt% and below. Cytotoxicity was noted at 0.05 wt% for all peptides. $(WR)_2$ and $(WR)_4$ were not tolerated at 0.0125 wt% by HDFa cells. This concentration is well below the CAC values (Fig. 1) and indicates that the self-assembled structures will be cytotoxic.

Conclusions

Our findings are summarized diagrammatically in Scheme 2. We find a rich variety of morphologies dependent on $(WR)_n$ sequence length, pH and concentration. There is a progressive tendency for extended β-sheet structures as the number of WR repeats increases, with fibril formation for $(WR)_3$ and wider/flatter nanotapes for $(WR)_4$ and $(WR)_5$. These are stable over a wide pH range (pH 2.5–12) for these latter peptides, which may be advantageous for applications where flat nanostructures are preferred. Our findings that β-sheet structures are stabilized for peptides with repeat alternating hydrophilic/hydrophobic residues are consistent with prior literature discussed in the Introduction.[2,3,5–7,11,25–27] However, there are significant interesting aspects of the pH-dependent phase behaviour for the shorter $(WR)_2$ and $(WR)_3$ peptides which both undergo LLPS *via* self-coacervation at pH 12. This is similar to our previous findings for W_2R_2 and W_3R_3, so for these short tryptophan/arginine peptides under these conditions the sequence type (alternating or blocky) does not affect LLPS. These peptides also show distinct behaviour in that their self-assembly is pH dependent, and micelles (at native pH 2.5 in water) or globular aggregates (in PBS) are observed for $(WR)_2$ whereas $(WR)_3$ forms twisted fibrils. We observe only LLPS droplet formation for 1 wt% $(WR)_3$ pH 12 and LLPS droplets + fibres for 3 wt% $(WR)_3$ at pH 12. It is very likely that for the latter sample, LLPS induces a local concentration above the CAC inside the coacervate droplets. This drives a portion of the peptide to self-assemble into fibres, consequently decreasing the local peptide concentration inside the LLPS droplets, which then co-exist in equilibrium with the self-assembled peptide fibres. Interesting aspects for future study include examining nucleation mechanisms and kinetics of fibril formation from coacervate droplets in more detail, when increasing concentration (as for $(WR)_3$), changing pH (pH drop) or simply as a function of aging time.

We have also explored conditions for hydrogel formation and find that these form under a range of conditions (in PBS and at pH 12) for the β-sheet forming $(WR)_4$ and $(WR)_5$ peptides. Spectroscopic methods (CD and FTIR) along with SAXS shows that the hydrogels are stabilized by a β-sheet nanotape network structure. At sufficiently high concentration, a hydrogel is also observed at pH 12 for $(WR)_3$, again underpinned by a fibril mesh. The cytocompatibility of the peptides to human dermal fibroblasts is excellent below 0.025 wt%. The peptides therefore hold promise for the future development of antimicrobial materials, indeed C-terminal capped $(WR)_2$

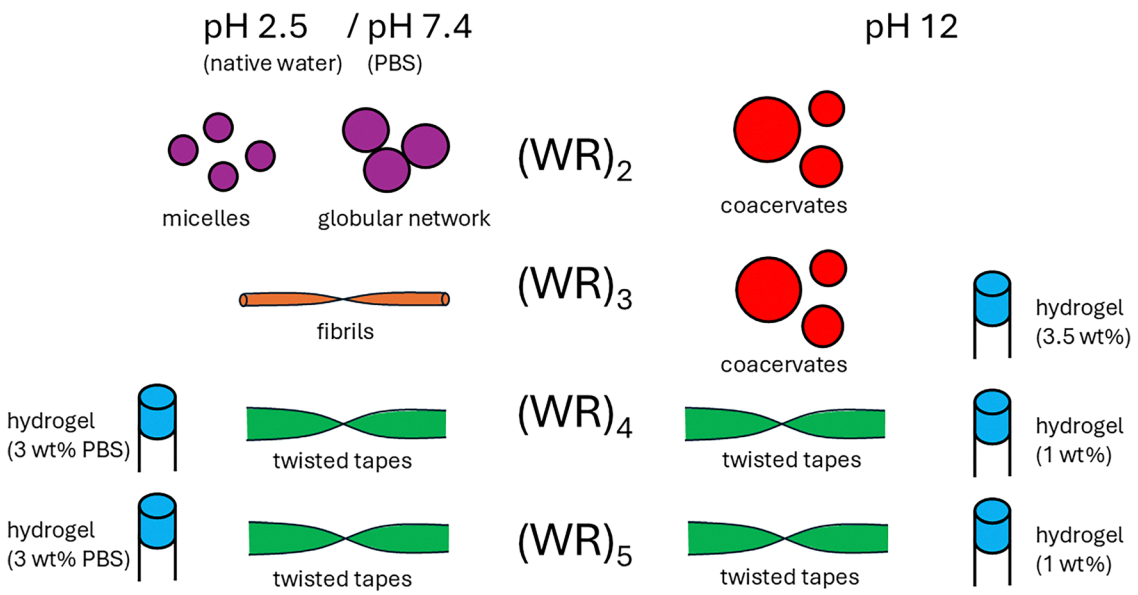

Scheme 2 Schematic of self-assembled structures observed for the $(WR)_n$ repeat peptides under the pH conditions shown, along with studied hydrogel formation conditions. It can be noted that a population of fibrils is also observed for $(WR)_3$ at pH 12 and the fibrillar network structure leads to hydrogel formation at higher concentration.

and $(WR)_3$ show very low minimum inhibitory concentrations against a range of Gram-positive and negative bacteria including disease-relevant pathogens such as MRSA,[65,66] as do other patterned α-helical tryptophan/arginine peptides.[67] We plan further studies examining the antimicrobial behaviour comparing uncapped and capped $(WR)_n$ repeat peptides and other variants. Such applications should consider that high concentrations favouring self-assembly also lead to cytotoxicity, but below the CAC these peptides may be useful for other applications such as tissue engineering. Samples undergoing LLPS at pH 12 may be of interest for potential applications in catalysis, for example.

Conflicts of interest

There are no conflicts to declare.

Data availability

The data is available upon reasonable request from the authors.

Supporting information (SI): tables of SAXS fit parameters, titration data, additional cryo-TEM, cryo-SEM and LSCM images, SAXS/WAXS and fiber XRD data, data from DLS, data for $(WR)_3$ pH 12 hydrogel. See DOI: **https://doi.org/10.1039/d5ma01006c**.

Acknowledgements

This work was supported by EPSRC Fellowship grant (reference EP/V053396/1) to IWH. We thank Diamond for the award of SAXS beamtime on B21 (ref. SM34342-5, SM27575-1 and SM35585-1) and Barbara Gerbelli, Nathan Cowieson and Nikul Khunti for assistance. We acknowledge use of the Chemical Analysis Facility at the University of Reading.

References

1 S. G. Zhang, T. Holmes, C. Lockshin and A. Rich, Spontaneous Assembly of a Self-Complementary Oligopeptide to Form a Stable Macroscopic Membrane, *Proc. Natl. Acad. Sci. U. S. A.*, 1993, **90**, 3334–3338.
2 S. G. Zhang, Discovery of the first self-assembling peptide, study of peptide dynamic behaviors, and G protein-coupled receptors using an Aviv circular dichroism spectropolarimeter, *Biopolymers*, 2018, **109**, e23235.
3 S. G. Zhang, Discovery and design of self-assembling peptides, *Interface Focus*, 2017, **7**, 20170028.
4 S. Sankar, K. O'Neill, M. B. D'Arc, F. Rebeca, M. Buffier, E. Aleksi, M. I. Fan, N. Matsuda, E. S. Gil and L. Spirio, Clinical Use of the Self-Assembling Peptide RADA16: A Review of Current and Future Trends in Biomedicine, *Front. Bioeng. Biotechnol.*, 2021, **9**, 679525.
5 A. Saiani, A. Mohammed, H. Frielinghaus, R. Collins, N. Hodson, C. M. Kielty, M. J. Sherratt and A. F. Miller, Self-assembly and gelation properties of alpha-helix versus beta-sheet forming peptides, *Soft Matter*, 2009, **5**, 193–202.
6 J. Gao, C. Tang, M. A. Elsawy, A. M. Smith, A. F. Miller and A. Saiani, Controlling Self-Assembling Peptide Hydrogel Properties through Network Topology, *Biomacromolecules*, 2017, **18**, 826–834.
7 M. A. Elsawy, J. K. Wychowaniec, L. A. C. Díaz, A. M. Smith, A. F. Miller and A. Saiani, Controlling Doxorubicin Release from a Peptide Hydrogel through Fine of Fiber Interactions, *Biomacromolecules*, 2022, **23**, 2624–2634.
8 D. Roberts, C. Rochas, A. Saiani and A. F. Miller, Effect of Peptide and Guest Charge on the Structural, Mechanical and Release Properties of beta-Sheet Forming Peptides, *Langmuir*, 2012, **28**, 16196–16206.
9 M. A. N. Soliman, A. Khedr, T. Sahota, R. Armitage, R. Allan, K. Laird, N. Allcock, F. I. Ghuloum, M. H. Amer, R. Alazragi, C. J. C. Edwards-Gayle, J. K. Wychowaniec, A. V. Vargiu and M. A. Elsawy, Unraveling the Atomistic Mechanism of Electrostatic Lateral Association of Peptide β-Sheet Structures and Its Role in Nanofiber Growth and Hydrogelation, *Small*, 2025, **21**, 2408213.
10 J. K. Wychowaniec, E. I. Bektas, M. Muerner, J. Sapudom, M. Srejber, M. Airoldi, R. Schmidt, A. J. Vernengo, C. J. C. Edwards-Gayle, P. S. Tipay, M. Otyepka, J. Teo, D. Eglin and M. D'Este, Effect of Tyrosine-Containing Self-Assembling β-Sheet Peptides on Macrophage Polarization and Inflammatory Response, *ACS Appl. Mater. Interfaces*, 2025, **17**, 27740–27758.
11 J. P. Schneider, D. J. Pochan, B. Ozbas, K. Rajogopal, L. Pakstis and J. Kretsinger, Responsive hydrogels from the intramolecular folding and self-assembly of a designed peptide, *J. Am. Chem. Soc.*, 2002, **124**, 15030–15037.
12 L. Haines-Butterick, K. Rajagopal, M. Branco, D. Salick, R. Rughani, M. Pilarz, M. S. Lamm, D. J. Pochan and J. P. Schneider, Controlling hydrogelation kinetics by peptide design for three-dimensional encapsulation and injectable delivery of cells, *Proc. Natl. Acad. Sci. U. S. A.*, 2007, **104**, 7791–7796.
13 R. A. Hule, R. P. Nagarkar, A. Altunbas, H. R. Ramay, M. C. Branco, J. P. Schneider and D. J. Pochan, Correlations between structure, material properties and bioproperties in self-assembled beta-hairpin peptide hydrogels, *Faraday Discuss.*, 2008, **139**, 251–264.
14 I. W. Hamley, *Introduction to Peptide Science*, Wiley, Chichester, 2020.
15 T. P. J. Knowles, C. A. Waudby, G. L. Devlin, S. I. A. Cohen, A. Aguzzi, M. Vendruscolo, E. M. Terentjev, M. E. Welland and C. M. Dobson, An Analytical Solution to the Kinetics of Breakable Filament Assembly, *Science*, 2009, **326**, 1533–1537.
16 S. I. A. Cohen, M. Vendruscolo, M. E. Welland, C. M. Dobson, E. M. Terentjev and T. P. J. Knowles, Nucleated polymerization with secondary pathways. I. Time evolution of the principal moments, *J. Chem. Phys.*, 2011, **135**, 065107.
17 S. I. A. Cohen, M. Vendruscolo, C. M. Dobson and T. P. J. Knowles, Nucleated polymerization with secondary pathways. II. Determination of self-consistent solutions to

growth processes described by non-linear master equations, *J. Chem. Phys.*, 2011, **135**, 065106.

18 S. I. A. Cohen, M. Vendruscolo, C. M. Dobson and T. P. J. Knowles, Nucleated polymerization with secondary pathways. III. Equilibrium behavior and oligomer populations, *J. Chem. Phys.*, 2011, **135**, 065105.

19 P. Zhou, R. R. Xing, Q. Li, J. B. Li, C. Q. Yuan and X. H. Yan, Steering phase-separated droplets to control fibrillar network evolution of supramolecular peptide hydrogels, *Matter*, 2023, **6**, 1945–1963.

20 C. Q. Yuan, R. R. Xing, J. Cui, W. Fan, J. B. Li and X. H. Yan, Multistep Desolvation as a Fundamental Principle Governing Peptide Self-Assembly Through Liquid-Liquid Phase Separation, *CCS Chem.*, 2024, **6**, 255–265.

21 R. Chang, C. Q. Yuan, P. Zhou, R. R. Xing and X. H. Yan, Peptide Self-assembly: From Ordered to Disordered, *Acc. Chem. Res.*, 2024, **57**, 289–301.

22 C. Q. Yuan, A. Levin, W. Chen, R. R. Xing, Q. L. Zou, T. W. Herling, P. K. Challa, T. P. J. Knowles and X. H. Yan, Nucleation and Growth of Amino Acid and Peptide Supramolecular Polymers through Liquid-Liquid Phase Separation, *Angew. Chem., Int. Ed.*, 2019, **58**, 18116–18123.

23 V. Castelletto, L. de Mello, E. R. da Silva, J. Seitsonen and I. W. Hamley, Comparison of the self-assembly and cytocompatibility of conjugates of Fmoc(9-fluorenylmethoxycarbonyl) with hydrophobic, aromatic, or charged amino acids, *J. Pept. Sci.*, 2024, **30**, e3571.

24 A. Jain, S. Kassem, R. S. Fisher, B. R. Wang, T. D. Li, Y. He, S. Elbaum-Garfinkle, R. Ulijn and T. Wang, Connected Peptide Modules Enable Controlled Co-Existence of Self-Assembled Fibers Inside Liquid Condensates, *J. Am. Chem. Soc.*, 2022, **144**, 15002–15007.

25 C. C. Decandio, E. R. Silva, I. W. Hamley, V. Castelletto, M. S. Liberato, C. L. P. Oliveira and W. A. Alves, Self-assembly of a designed alternating arginine/phenylalanine oligopeptide, *Langmuir*, 2015, **31**, 4513–4523.

26 E. R. Silva, E. Listik, S. W. Han, W. A. Alves, B. M. Soares, M. Reza, J. Ruokolainen and I. W. Hamley, Sequence length dependence in arginine/phenylalanine oligopeptides: implications for self-assembly and cytotoxicity, *Biophys. Chem.*, 2018, **233**, 1–12.

27 L. R. Mello, I. W. Hamley, A. Miranda, W. A. Alves and E. R. Silva, β-sheet assembly in amyloidogenic glutamic acid nanostructures: insights from X-ray scattering and infrared nanospectroscopy, *J. Pept. Sci.*, 2019, **25**, e3170.

28 V. Castelletto, J. Seitsonen, A. Pollitt and I. W. Hamley, Minimal Peptide Sequences That Undergo Liquid-Liquid Phase Separation via Self-Coacervation or Complex Coacervation with ATP, *Biomacromolecules*, 2024, **25**, 5321–5331.

29 N. P. Cowieson, C. J. C. Edwards-Gayle, K. Inoue, N. S. Khunti, J. Doutch, E. Williams, S. Daniels, G. Preece, N. A. Krumpa, J. P. Sutter, M. D. Tully, N. J. Terrill and R. P. Rambo, Beamline B21: high-throughput small-angle X-ray scattering at Diamond Light Source, *J. Synchrotron Radiat.*, 2020, **27**, 1438–1446.

30 C. J. C. Edwards-Gayle, N. Khunti, I. W. Hamley, K. Inoue, N. Cowieson and R. Rambo, Design of a multipurpose sample cell holder for the Diamond Light Source high-throughput SAXS beamline B21, *J. Synchrotron Radiat.*, 2021, **28**, 318–321.

31 I. W. Hamley, *Small-Angle Scattering: Theory, Instrumentation, Data and Applications*, Wiley, Chichester, 2021.

32 A. Guinier and G. Fournet, *Small angle scattering of X-rays*, Wiley, New York, 1955.

33 G. Porod, in *Small-Angle X-ray Scattering*, ed. O. Glatter and O. Kratky, Academic Press, London, 1982, ch. 2, pp. 17–51.

34 G. Pabst, M. Rappolt, H. Amenitsch and P. Laggner, Structural information from multilamellar liposomes at full hydration: full *q*-range fitting with high quality X-ray data, *Phys. Rev. E: Stat. Phys., Plasmas, Fluids, Relat. Interdiscip. Top.*, 2000, **62**, 4000–4009.

35 A. Caillé, X-Ray Scattering by Smectic-A Crystals, *C. R. Seances Acad. Sci., Ser. B*, 1972, **274**, 891–893.

36 I. Bressler, J. Kohlbrecher and A. F. Thünemann, SASfit: a tool for small-angle scattering data analysis using a library of analytical expressions, *J. Appl. Crystallogr.*, 2015, **48**, 1587–1598.

37 J. Kohlbrecher and I. Bressler, Updates in SASfit for fitting analytical expressions and numerical models to small-angle scattering patterns, *J. Appl. Crystallogr.*, 2022, **55**, 1677–1688.

38 O. S. Makin, P. Sikorski and L. C. Serpell, CLEARER: a new tool for the analysis of X-ray fibre diffraction patterns and diffraction simulation from atomic structural models, *J. Appl. Crystallogr.*, 2007, **40**, 966–972.

39 S. W. Provencher, Inverse problems in polymer characterization: direct analysis of polydispersity with photon correlation spectroscopy, *Makromol. Chem.*, 1979, **180**, 201–209.

40 H. LeVine, Thioflavine T interaction with synthetic Alzheimer's disease β-amyloid peptides: detection of amyloid aggregation in solution, *Protein Sci.*, 1993, **2**, 404–410.

41 H. LeVine, in *Methods in Enzymology*, ed. R. Wetzel, Academic Press, San Diego, 1999, vol. 309, pp. 274–284.

42 L. Alderighi, P. Gans, A. Ienco, D. Peters, A. Sabatini and A. Vacca, Hyperquad simulation and speciation (HySS): a utility program for the investigation of equilibria involving soluble and partially soluble species, *Coord. Chem. Rev.*, 1999, **184**, 311–318.

43 A. Roy, P. Bour and T. A. Keiderling, TD-DFT Modeling of the Circular Dichroism for a Tryptophan Zipper Peptide with Coupled Aromatic Residues, *Chirality*, 2009, **21**, E163–E171.

44 N. Amdursky and M. M. Stevens, Circular Dichroism of Amino Acids: Following the Structural Formation of Phenylalanine, *ChemPhysChem*, 2015, **16**, 2768–2774.

45 A. Rodger and B. Nordén, *Circular dichroism and linear dichroism*, Oxford University Press, Oxford, 1997.

46 B. Nordén, A. Rodger and T. R. Dafforn, *Linear Dichroism and Circular Dichroism: A Textbook on Polarized-Light Spectroscopy*, RSC, Cambridge, 2010.

47 V. Castelletto, C. J. C. Edwards-Gayle, I. W. Hamley, J. N. B. D. Pelin, W. A. Alves, A. M. Alguilar, J. Seitsonen

and J. Ruokolainen, Self-Assembly of a Catalytically Active Lipopeptide and its Incorporation into Cubosomes, *ACS Appl. Bio Mater.*, 2019, **2**, 3639–3648.

48 V. Castelletto, C. J. C. Edwards-Gayle, I. W. Hamley, G. Barrett, J. Seitsonen, J. Ruokolainen, L. R. de Mello and E. R. da Silva, Model self-assembling arginine-based tripeptides show selective activity against Pseudomonas bacteria, *Chem. Commun.*, 2020, **56**, 615–618.

49 P. Haris and D. Chapman, The conformational analysis of peptides using Fourier Transform IR spectroscopy, *Biopolymers*, 1995, **37**, 251–263.

50 J. T. Pelton and L. R. McLean, Spectroscopic methods for analysis of protein secondary structure, *Anal. Biochem.*, 2000, **277**, 167–176.

51 H. Gaussier, H. Morency, M. C. Lavoie and M. Subirade, Replacement of trifluoroacetic acid with HCl in the hydrophobic purification steps of pediocin PA-1: a structural effect, *Appl. Environ. Microbiol.*, 2002, **68**, 4803–4808.

52 F. Eker, K. Griebenow and R. Schweitzer-Stenner, $A\beta_{1-28}$ fragment of the amyloid peptide predominantly adopts a polypropyline II conformation in acidic solution, *Biochemistry*, 2004, **43**, 6893–6898.

53 A. Barth, The infrared absorption of amino acid side chains, *Prog. Biophys. Mol. Biol.*, 2000, **74**, 141–173.

54 A. Barth, Infrared spectroscopy of proteins, *Biochim. Biophys. Acta, Bioenerg.*, 2007, **1767**, 1073–1101.

55 B. Stuart, *Biological Applications of Infrared Spectroscopy*, Wiley, Chichester, 1997.

56 R. W. Woody, in *Circular Dichroism. Principles and Applications*, ed. K. Nakanishi, N. Berova and R. W. Woody, VCH, New York, 1994, pp. 473–496.

57 S. M. Kelly, T. J. Jess and N. C. Price, How to study proteins by circular dichroism, *Biochim. Biophys. Acta*, 2005, **1751**, 119–139.

58 L. C. Serpell, Alzheimer's amyloid fibrils: structure and assembly, *Biochim. Biophys. Acta*, 2000, **1502**, 16–30.

59 I. W. Hamley, Peptide fibrillisation, *Angew. Chem.*, 2007, **46**, 8128–8147.

60 P. J. Flory, *Statistical Mechanics of Chain Molecules*, John Wiley, New York, 1969.

61 P. G. de Gennes, *Scaling Concepts in Polymer Physics*, Cornell University Press, Ithaca, 1979.

62 I. W. Hamley, *Introduction to Soft Matter*, Wiley, Chichester, Revised edn, 2007.

63 T. Bernas and J. Dobrucki, Mitochondrial and nonmitochondrial reduction of MTT: interaction of MTT with TMRE, JC-1, and NAO mitochondrial fluorescent probes, *Cytometry*, 2002, **47**, 236–242.

64 M. Ghasemi, T. Turnbull, S. Sebastian and I. Kempson, The MTT Assay: Utility, Limitations, Pitfalls, and Interpretation in Bulk and Single-Cell Analysis, *Int. J. Mol. Sci.*, 2021, **22**, 12827.

65 R. N. Murugan, B. Jacob, E. H. Kim, M. Ahn, H. Sohn, J. H. Seo, C. Cheong, J. K. Hyun, K. S. Lee, S. Y. Shin and J. K. Bang, Non hemolytic short peptidomimetics as a new class of potent and broad-spectrum antimicrobial agents, *Bioorg. Med. Chem. Lett.*, 2013, **23**, 4633–4636.

66 Q. Y. Lau, F. M. Ng, J. W. D. Cheong, Y. Y. A. Yap, Y. Y. F. Tan, R. Jureen, J. Hill and C. S. B. Chia, Discovery of an ultra-short linear antibacterial tetrapeptide with anti-MRSA activity from a structure-activity relationship study, *Eur. J. Med. Chem.*, 2015, **105**, 138–144.

67 B. Deslouches, J. D. Steckbeck, J. K. Craigo, Y. Doi, T. A. Mietzner and R. C. Montelaro, Rational Design of Engineered Cationic Antimicrobial Peptides Consisting Exclusively of Arginine and Tryptophan, and Their Activity against Multidrug-Resistant Pathogens, *Antimicrob. Agents Chemother.*, 2013, **57**, 2511–2521.